



Equilibrium evolution in oscillating-field current-drive experiments

K. J. McCollam, J. K. Anderson, A. P. Blair, D. Craig, D. J. Den Hartog et al.

Citation: [Phys. Plasmas](#) **17**, 082506 (2010); doi: 10.1063/1.3461167

View online: <http://dx.doi.org/10.1063/1.3461167>

View Table of Contents: <http://pop.aip.org/resource/1/PHPAEN/v17/i8>

Published by the [American Institute of Physics](#).

Additional information on Phys. Plasmas

Journal Homepage: <http://pop.aip.org/>

Journal Information: http://pop.aip.org/about/about_the_journal

Top downloads: http://pop.aip.org/features/most_downloaded

Information for Authors: <http://pop.aip.org/authors>

ADVERTISEMENT

An advertisement banner for AIP Advances. The background is a green and white abstract pattern of curved lines. In the center, the text 'AIP Advances' is written in a green font, with a series of orange circles of varying sizes above it. Below this, the text 'Special Topic Section: PHYSICS OF CANCER' is written in white on a dark green background. At the bottom, the text 'Why cancer? Why physics?' is written in white, followed by a blue button with the text 'View Articles Now' in white.

AIP Advances

Special Topic Section:
PHYSICS OF CANCER

Why cancer? Why physics? [View Articles Now](#)

Equilibrium evolution in oscillating-field current-drive experiments

K. J. McCollam,¹ J. K. Anderson,¹ A. P. Blair,¹ D. Craig,¹ D. J. Den Hartog,¹ F. Ebrahimi,¹ R. O'Connell,¹ J. A. Reusch,¹ J. S. Sarff,¹ H. D. Stephens,¹ D. R. Stone,¹ D. L. Brower,² B. H. Deng,^{2,a)} and W. X. Ding²

¹Department of Physics, University of Wisconsin-Madison, Madison, Wisconsin 53706, USA

²Department of Physics and Astronomy, University of California at Los Angeles, Los Angeles, California 90095, USA

(Received 23 April 2010; accepted 17 June 2010; published online 20 August 2010)

Oscillating-field current drive (OFCD) is a proposed method of steady-state toroidal plasma sustainment in which ac poloidal and toroidal loop voltages are applied to produce a dc plasma current. OFCD is added to standard, inductively sustained reversed-field pinch plasmas in the Madison Symmetric Torus [R. N. Dexter *et al.*, Fusion Technol. **19**, 131 (1991)]. Equilibrium profiles and fluctuations during a single cycle are measured and analyzed for different relative phases between the two OFCD voltages and for OFCD off. For OFCD phases leading to the most added plasma current, the measured energy confinement is slightly better than that for OFCD off. By contrast, the phase of the maximum OFCD helicity-injection rate also has the maximum decay rate, which is ascribed to transport losses during discrete magnetic-fluctuation events induced by OFCD. Resistive-magnetohydrodynamic simulations of the experiments reproduce the observed phase dependence of the added current. © 2010 American Institute of Physics. [doi:10.1063/1.3461167]

I. INTRODUCTION

Oscillating-field current drive¹ (OFCD) is a proposed method of plasma-current sustainment, primarily conceived for the reversed-field pinch (RFP),² in which applied ac poloidal and toroidal loop voltages interact with magnetic relaxation to produce a dc plasma current. Since, unlike the standard toroidal induction, it does not rely on poloidal magnetic flux buildup, OFCD would be a (quasi-) steady-state method, which is otherwise problematic for the RFP owing to its small neoclassical bootstrap current. Ideally OFCD would be capable of relatively high current-drive efficiency at high plasma temperature compared to rf-wave or neutral-beam injection due to its inductive nature,³ which would also allow global current drive without the need for wall access ports. However, even if the current drive is efficient, its reliance on relaxation may cause enough outward thermal transport due to stochasticity associated with magnetic fluctuations to impair OFCD's feasibility in maintaining high plasma temperature in a steady state. While improved confinement has been achieved transiently in experimental RFPs sustained by toroidal induction,⁴ future RFP development calls for an optimized, practical strategy for efficient sustainment with good confinement, and so both the topics of OFCD's effectiveness and its confinement properties are important. More generally the interaction between control methods such as current drive and plasma responses such as relaxation and transport is an important topic throughout magnetic-confinement research that OFCD exhibits in a unique way.

The OFCD concept was introduced in terms of helicity balance. Magnetic helicity $K = \int \mathbf{A} \cdot \mathbf{B} dv$ is related to the

linkage of flux of the magnetic field $\mathbf{B} = \nabla \times \mathbf{A}$ within a volume v .⁵ For a given profile the plasma current tends to increase with increasing K , and so helicity injection is a type of current drive. The time derivative can be written as $dK/dt = 2(V_\phi \Phi - \int \eta \mathbf{J} \cdot \mathbf{B} dv)$ with an inductive injection term due to a toroidal loop voltage V_ϕ applied on the toroidal flux Φ , and a resistive decay term, where η is the resistivity and $\mathbf{J} \propto \nabla \times \mathbf{B}$ the current density. In OFCD an oscillating poloidal loop voltage $V_\theta = \hat{V}_\theta \sin \omega t$ induces an oscillating Φ on which an oscillating $V_\phi = \hat{V}_\phi \sin(\omega t - \delta)$ is applied, leading to an oscillating helicity-injection rate with a cycle-average component $2\langle V_\phi \Phi \rangle = (\hat{V}_\phi \hat{V}_\theta / \omega) \sin \delta$ to counter-resistive decay. The maximum helicity-injection rate occurs for the phase $\delta = \pi/2$ and maximum ejection for $\delta = -\pi/2$.

In ZT-40M experiments OFCD was observed to drive an additional $\sim 5\%$ of the RFP plasma current when added to the toroidal induction,⁶ in what is called partial OFCD. The addition was found to be limited by plasma-wall interactions associated with the highest of the applied input power levels. Tests of OFCD on tokamaks have not conclusively yielded current drive, which for some experiments was ascribed to a lack of sufficient relaxation in the strong tokamak toroidal magnetic field,⁷ and in others to nonoptimal hardware configuration.⁸ Previously reported experiments on the Madison Symmetric Torus (MST) RFP (Ref. 9) have shown a 5%–10% current increase maximized with a positive but nonmaximal OFCD helicity injection at an optimal $\delta \approx \pi/8$.¹⁰ The amount of added current is roughly consistent with predictions from one-dimensional (1D) magnetic-energy balance¹¹ or a simple helicity balance, while accurately modeling the phase dependence requires more complex treatment since the observed optimum is not $\delta = \pi/2$, the phase of maximum helicity injection. In the optimal $\delta \approx \pi/8$ case magnetic fluctuations with poloidal mode num-

^{a)}Present address: Tri Alpha Energy Inc., 19631 Pauling, Foothill Ranch, CA 92610.

ber $m=0$ are slightly smaller on average than for the standard RFP without OFCD. It is concluded that a combination of OFCD helicity injection and a small confinement improvement and drop in resistance, leading to additional current driven by the background toroidal induction, might explain the increase. Plasma-wall interactions have not been identified as a major limiting factor in those experiments.

This paper reports on an experimental study of partial OFCD on the MST device using internal measurements. The main topic is a comparison of five different cases: OFCD with $\delta=\pi/2$, $\pi/4$, 0, and $-\pi/2$, and OFCD off. The measured evolution of electromagnetic and thermal equilibrium quantities in the OFCD plasmas over a single cycle is detailed and analyzed. A main result is that for the OFCD cases of $\delta=\pi/4$ and $\delta=0$, which are near the previously observed optimal phase for current addition, the energy-confinement time calculated using electron measurements is observed to be slightly improved compared to the OFCD-off case. Also, for the $\delta=\pi/2$ case, whose added current is relatively small despite its maximum helicity-injection rate, the helicity-decay rate is maximum. This is mostly due to increased resistance caused by relatively poor confinement associated with discrete magnetic-fluctuation events induced by the applied oscillations. Nonlinear, three-dimensional (3D) resistive-MHD (-magnetohydrodynamic) simulations that used experimental parameters are compared to previous experimental results, and the phase dependences of added plasma current agree.

A. Background

Building on earlier numerical studies,^{12,13} full sustainment of the RFP was simulated in 3D, nonlinear, resistive-MHD calculations that also revealed in more detail the role of relaxation in OFCD.¹¹ The axisymmetric applied oscillations produce a cycle-average electromotive force (EMF) $\langle \mathbf{U} \times \mathbf{B} \rangle_{\parallel}$ parallel to the cycle average $\langle \mathbf{B} \rangle$, where \mathbf{U} is a plasma-flow velocity.¹⁴ This source EMF drives edge plasma current and destabilizes nonaxisymmetric magnetic fluctuations, which induce their own net EMF that drives current throughout the volume, including the core. Thus is the radial profile of normalized parallel-current density $\lambda \propto J_{\parallel}/B$ driven toward being hollow by the source and flattened by relaxation, as is consistent with basic relaxation theory.¹⁵ The calculated fluctuation spectrum included modes resonant outside the reversal surface not present in a standard RFP, while the total fluctuation energy was similar to that for the standard case.

The size of OFCD modulations needed for full sustainment was found to be large. The calculations were done with Lundquist numbers $S \equiv \tau_{\text{res}}/\tau_A$, where τ_{res} is the resistive-diffusion time and τ_A is the Alfvén time, of up to $S=5 \times 10^5$, which is somewhat smaller, connoting lower plasma conductivity, than values attainable in present experiments. The required modulation was around half of the equilibrium value, while a weakly decreasing scaling of its relative amplitude with higher S was also derived. Such fractions present experimental challenges in addition to that of simply providing the needed source power, which is itself at the

limit of feasibility for present devices. With transport, the modulations and associated magnetic fluctuations may result in conductivity so low that the OFCD input is dissipated rather than acting to increase the net current. Present OFCD experiments focus on the partial sustainment tests that are feasible given hardware capability and plasma S values.

The fundamental reliance of OFCD on magnetic relaxation, which involves field-line reconnection and some degrees of magnetic stochasticity, causes concern about its confinement properties, but the confinement for OFCD has not been modeled. It might be guessed to be similar to that for the standard RFP sustained by toroidal induction, for which scalings have been derived from numerical calculations with S up to present experimental values.¹⁶ Toroidal induction is anticurrent drive in the edge of a RFP and current drive in the core, and continually drives the plasma toward resistive-tearing instability, leading to a relaxation cycle. By contrast the OFCD source tends to drive current in the edge and vanishes in the core where relaxation drives net current. Previous experiments¹⁰ and MHD calculations¹⁷ both indicate a degree of fluctuation suppression by current-profile modification in partial OFCD. In oscillating poloidal current drive experiments, a V_{θ} oscillation alone has been applied in order to control fluctuations and improve the global energy confinement over that of the standard RFP discharge.^{18,19} These points might suggest that confinement properties in full OFCD could be different than in toroidal induction.

II. EXPERIMENTS

Data were obtained from several MST pulses for each of five cases: a standard, inductively sustained RFP with OFCD added for the four phases $\delta=\pi/2$, $\pi/4$, 0, and $-\pi/2$ (progressing from maximum positive to negative OFCD helicity-injection rates), and the same baseline RFP with OFCD off. The two OFCD voltages were provided by twin precharged tank (LC) circuits each tuned to resonate at $f \approx 280$ Hz, powered by pulse-forming networks, switched by commutating ignitrons, and coupled inductively to MST's poloidal and toroidal field circuits.²⁰ For OFCD pulses the poloidal loop voltage V_{θ} oscillation was always triggered at the same shot time (15 ms) and the trigger for the toroidal loop voltage V_{ϕ} oscillation was varied around that to obtain a particular δ value. With fixed power-supply settings, the amplitudes of the applied oscillating voltages were $\hat{V}_{\phi} \approx 100$ V and $\hat{V}_{\theta} \approx 10$ V, compared to MST's typical $V_{\phi} \approx 25$ V for the standard toroidal induction and $V_{\theta} \approx 1$ V. As the aspect ratio of major to minor radius for MST is $R_0/a=1.5$ m/0.52 m ≈ 3 , the amplitudes of the OFCD toroidal and poloidal electric-field components are thus related by $\hat{E}_{\phi} \approx 3\hat{E}_{\theta}$. The plasma density was controlled with preprogrammed gas puffing and targeted to the same desired flattop level for every pulse.

Standard operational data signals sampled at ≥ 100 kHz are the toroidal plasma current I_{ϕ} , edge toroidal magnetic field $B_{\phi}(a)$, toroidal magnetic flux Φ , loop voltages V_{ϕ} and V_{θ} , central chord-average electron density \bar{n}_e , and edge magnetic-fluctuation amplitudes for modes with poloidal mode numbers $m=0$ and $m=1$. Far-infrared (FIR) interferometry²¹ and polarimetry²² were used to measure av-

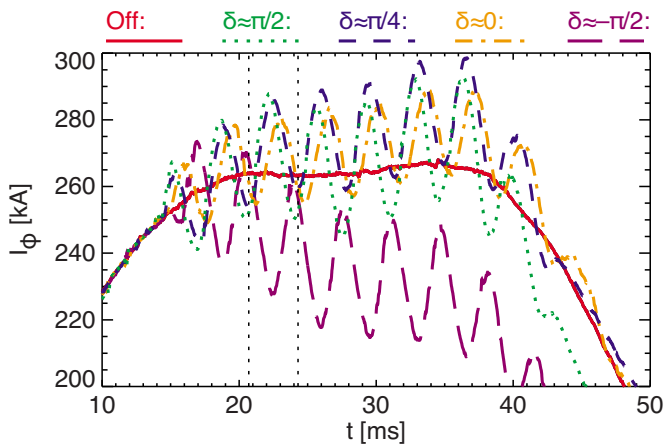


FIG. 1. (Color online) Time dependences of the plasma current I_ϕ in the cases of OFCD off (red solid) and OFCD on at $\delta \approx \pi/2$ (green dotted), $\delta \approx \pi/4$ (blue dashed), $\delta \approx 0$ (orange dashed-dotted), and $\delta \approx -\pi/2$ (purple long-dashed) for pulse ensembles similar to those analyzed in this paper. To match all the I_ϕ values before the start of OFCD at 15 ms, each OFCD waveform has been shifted up or down by a small constant according to its ensemble's statistical variation. The time window examined in this paper is indicated by vertical dotted lines.

eraged electron density and vertical magnetic field, respectively, on 11 internal chords time resolved at 250 kHz. Motional-Stark-effect (MSE) spectroscopy²³ was used to measure the core toroidal magnetic field at one location once per pulse. Thomson-scattering (TS) spectroscopy²⁴ was used to measure electron temperature T_e at 14 radial locations across the plasma twice per pulse.

III. DATA ANALYSIS

A. Data ensembles

For each of the five experimental cases, the same time window corresponding to the third cycle in the OFCD pulse, from 20.7 to 24.3 ms in shot time, is analyzed. This cycle is chosen in order to study fully developed OFCD at the beginning of the equilibrium flattop (as can be seen in Fig. 1 nearby). Plasma equilibria for seven time points (every 0.6 ms spread over the 3.6 ms cycle) on this window are reconstructed with the MSTFIT code²⁵ using the data listed above. The data set used is composed of around two dozen MST pulses for each of the five ensembles, selected from a larger set of pulses to have matching I_ϕ and V_ϕ before the OFCD start time and average \bar{n}_e during the time window. Standard operational signals and the FIR signals from ensembles of individual pulses are averaged over 0.25 ms windows centered on the seven time points, which are covered by MSE and TS measurements averaged over the course of the run. Statistical uncertainties for the various data are dominated by pulse-to-pulse variations, whose relative values are around 5% for magnetic data including the MSE and around 10% for density and TS data. These are propagated using the number of measurements at each time and, for cycle averages, the number of time points in the cycle.

For OFCD cases, sawteeth are entrained to occur at the same phase of each cycle, most often between two measurement times. In the case of OFCD off, ensemble averaging

effectively averages over the quasiperiodic relaxation cycle punctuated by sawtooth magnetic-fluctuation events, which means signals from that ensemble correspond to running sawtooth-cycle averages.

B. Equilibrium reconstructions

Toroidally symmetric magnetostatic equilibria, with $\mathbf{J} \times \mathbf{B} = \nabla p$, are reconstructed using the MSTFIT code,²⁵ which uses an algorithm of interleaved equilibrium calculations and fitting to available measurements. The reconstructions use a two-parameter power model for the normalized poloidal current $F(\psi)$ and a four-parameter fixed-point spline model for the plasma thermal pressure $p(\psi)$, both functions of poloidal magnetic flux per radian ψ . For each time point for each ensemble, the reconstructed equilibrium magnetic field \mathbf{B} , current density \mathbf{J} , and p are specified in the plasma region on a regular grid of points of major-radial R and vertical Z coordinates in a cylindrical coordinate system (R, ϕ, Z) with toroidal angle ϕ . The pressure is assumed to be twice the measured electron pressure ($p \equiv 2p_e$), which for these plasmas has only a small effect on the reconstructions. A divergenceless magnetic vector potential $\mathbf{A} = A_\theta + \psi \nabla \phi$ is calculated from the reconstruction with the poloidal component $A_\theta = A_R \mathbf{e}_R + A_Z \mathbf{e}_Z$ derived from the toroidal field B_ϕ by elliptic integrals.²⁶ The neoclassical scalar electrical resistivity η is calculated in the reconstruction²⁷ and depends on the effective ion charge Z_{eff} assumed to have a uniform, constant value of 2. A statistical uncertainty in $\eta \sim T_e^{-3/2}$ is propagated from that in T_e .

To augment these full equilibrium reconstructions, relaxed-state equilibria are calculated from surface measurements with a 1D cylindrical model.²⁸ Here the minor-radial r profile of the normalized parallel-current density $\lambda \equiv \mu_0 J_\parallel / B$ is assumed to follow a two-parameter power model $\lambda(r) = \lambda_0 [1 - (r/a)^\alpha]$, where a is the wall radius, λ_0 is the core value of λ , and α is a flatness parameter which is higher for a flatter λ profile. A fixed normalized thermal-pressure profile quadratic in r is assumed with a central peak of 7% of the local magnetic pressure.

C. Electric-field calculations

The equilibrium inductive electric field is calculated as $\mathbf{E}(t) = -\partial \mathbf{A}(t) / \partial t + [V_\phi(t) / 2\pi] \nabla \phi$, whose first term comes from the reconstructed vector potential and whose last term accounts for the changing poloidal flux in the Ohmic transformer, which is not part of the equilibrium reconstruction. At each spatial point the seven-point time series for each of the three components of $\mathbf{A}(t)$ is separately fit by least-squares to functional forms, $A(t) = A_0 + A_1 t + A_2 \sin(2\pi f t) + A_3 \cos(2\pi f t)$ for the OFCD cases, where f is fixed at the applied ac frequency, and $A(t) = A_0 + A_1 t$ for the OFCD-off case. From these the corresponding $\mathbf{E}(t)$ components are found by analytical differentiation. This method is similar in principle to those used in previous studies.^{27,29} Relative statistical uncertainties for the components of \mathbf{A} are assumed to be at least 2%, which is about the standard error of the mean for the ensemble-averaged magnetic measurements used in the equilibrium reconstructions. The values of

reduced chi-squared (χ_r^2) characterizing fit quality for the components of \mathbf{A} vary across the components, the plasma, and the different ensembles, and have a mean less than 1 with a small population up to around 5 and a large population at a few tenths (which implies some overestimation of statistical errors). Relative propagated errors in the components of \mathbf{E} are in the neighborhood of 20% of typical values for OFCD ensembles, for which they dominate other uncertainties.

IV. EXPERIMENTAL RESULTS

A. Global quantities

This section describes the main global behavior observed in the experiments. Adding OFCD to the RFP plasma adds to or subtracts from the plasma current I_ϕ according to the chosen phase δ between the two oscillators. Examples for previous experiments similar to those analyzed below are shown in Fig. 1. The OFCD is on from a shot time of 15 ms until around 40 ms, and the time window of interest for this paper starts at 20.7 ms and ends at 24.3 ms, which covers roughly the third OFCD cycle, near the start of the I_ϕ flat top, and which is indicated by vertical dotted lines in the figure. The examples from previous tests are shown here because in the present experiments the OFCD circuits did not provide good phase control and reliable commutation after this time window, and so the resulting plasma currents would not accurately reflect typical OFCD behavior over several cycles. However, qualitatively the observed phase dependences were similar to the previous.¹⁰ Of the OFCD phases used here, the most current is added for $\delta \approx \pi/4$ and the most subtracted for $\delta \approx -\pi/2$.

Zooming in to the time window of interest in the present experiments, the global signals I_ϕ , edge toroidal magnetic field $B_\phi(a)$, toroidal magnetic flux Φ , toroidal and poloidal loop voltages V_ϕ and V_θ , and central chord-average electron density \bar{n}_e for the five ensembles are shown in Fig. 2. The phase of optimum added I_ϕ , $\delta \approx \pi/8$,¹⁰ is not itself represented, but is bracketed by the nearby $\delta=0$ and $\delta=\pi/4$ cases. Over a single OFCD cycle, the net added I_ϕ for these phases is negligible, and the single-cycle dynamics are the topic of interest. In OFCD the I_ϕ oscillation tends to follow the applied V_ϕ oscillation inductively, as $B_\phi(a)$ tends to follow V_θ [which $\Phi(t) \equiv \int V_\theta(t) dt$ does by definition].

Sawtooth magnetic-relaxation events, entrained to the OFCD cycles, are evidenced by positive spikes in V_θ clustered around the initial and final time points in the time window, corresponding to rapid increases in Φ as negatively directed toroidal flux is expelled. These events are discrete bursts of magnetic relaxation associated with fluctuation-induced electromotive effect responsible for maintaining field reversal in a RFP sustained by toroidal induction.³⁰

Compared to the other phases the $\delta=-\pi/2$ case shows a larger net change in I_ϕ over the single cycle; for the same OFCD source levels, anticurrent drive is more effective than current drive. Its $B_\phi(a)$ and Φ oscillations appear to have nonsinusoidal features likely due to the large entrained sawtooth [at ~ 23.5 ms in Fig. 2(e)]. Also the cycle-average loop voltage $\langle V_\phi \rangle$ increases in this case. It is not as easily seen for

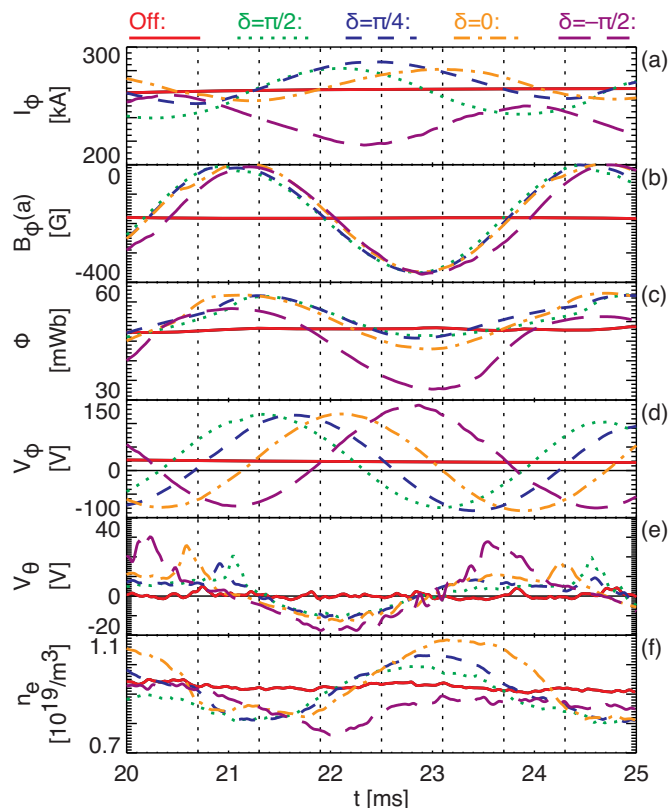


FIG. 2. (Color online) Time dependences including a single OFCD period of the plasma current I_ϕ (a), edge toroidal magnetic field $B_\phi(a)$ (b), toroidal magnetic flux Φ (c), toroidal loop voltage V_ϕ (d), poloidal loop voltage V_θ (e), and central chord-average electron density \bar{n}_e (f) for pulse ensembles with OFCD off (red solid) and OFCD on at $\delta=\pi/2$ (green dotted), $\delta=\pi/4$ (blue dashed), $\delta=0$ (orange dashed-dotted), and $\delta=-\pi/2$ (purple long-dashed). Time points for equilibrium reconstructions are indicated by vertical dotted lines.

the other phases, but $\langle V_\phi \rangle$ is minimized around $\delta=\pi/4$ and $\delta=0$, typically a few volts below the value for the OFCD-off case.

B. Magnetic fluctuations and equilibrium profile evolution

OFCD strongly affects magnetic fluctuations, both by entraining sawtooth relaxation events and by modulating the fluctuation activity between sawteeth, which is the main topic of this section. First the basic effects of the OFCD cycle and of the sawtooth cycle on the equilibria are compared, and then the interaction between OFCD, the equilibrium profiles, and magnetic activity is examined. Last the evolution of the vector components of the equilibrium magnetic field itself is shown.

In Fig. 3, the two plots show magnetic-fluctuation amplitudes measured at the wall for $m=1$ and $m=0$ modes, respectively, for the various ensembles. For each ensemble, the $m=1$ amplitude is the quadrature sum of the corresponding toroidal modes $5 \leq n \leq 15$, which are resonant in the core, and the $m=0$ amplitude is that of the corresponding $1 \leq n \leq 4$ modes, which are resonant at the reversal surface near the plasma edge.

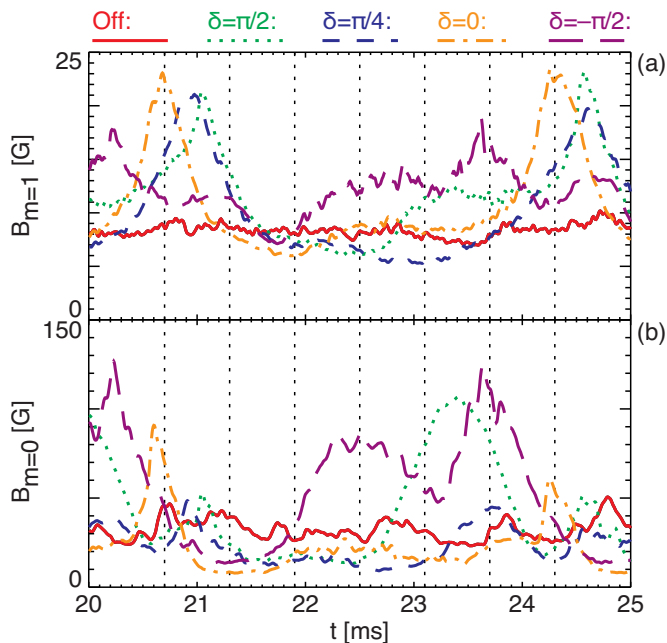


FIG. 3. (Color online) Time dependences including a single OFCD period of the $m=1$ ($5 \leq n \leq 15$) mode (a) and $m=0$ ($1 \leq n \leq 4$) mode magnetic-fluctuation amplitudes (b) for pulses ensembles with OFCD off (red solid) and OFCD on at $\delta = \pi/2$ (green dotted), $\delta = \pi/4$ (blue dashed), $\delta = 0$ (orange dashed-dotted), and $\delta = -\pi/2$ (purple long-dashed). Time points for equilibrium reconstructions are indicated by vertical dotted lines.

The sawteeth entrained by OFCD are visible in these ensembles as the large spikes in mode amplitude peaking before ~ 21.3 ms and after ~ 23.5 ms in Fig. 3. Note that, since the phase of sawtooth entrainment is not exactly the same every cycle, for the OFCD cases ensemble averaging damps the peak sawtooth fluctuation amplitude that would be observed in a single pulse, in these cases by a factor of about 2–3. For the OFCD-off ensemble, whose governing relaxation cycle is pseudoperiodic, individual sawtooth peaks have been averaged out almost completely. The natural sawtooth-cycle period for these pulses is around 4–5 ms, a bit longer than the OFCD period of 3.6 ms. The cycle-average fluctuation amplitudes during OFCD are minimized for phases around $\delta = 0$ and $\delta = \pi/4$. For these phases the $m=0$ amplitudes are slightly smaller than the corresponding time average for OFCD off, and the $m=1$ slightly larger.

It is interesting that as δ is changed by increasing the trigger time for the V_ϕ oscillator with the V_θ oscillator fixed, the times of OFCD-entrained sawtooth events decrease. This is visible in Fig. 3 where as δ goes from $\pi/2$ to $-\pi/2$ the early entrained sawteeth occur at times going from larger to smaller, from ~ 21.1 to ~ 20.3 ms, respectively. It implies that the sawteeth are entrained to the phase of V_θ referenced to that of V_ϕ , rather than to either of their absolute phases.

For OFCD cases, most significantly for $\delta = \pi/2$ and $\delta = -\pi/2$, there is also substantial mode activity for both $m=0$ and $m=1$ between sawteeth associated with the OFCD cycle, which will be called intersawtooth activity in this paper. These are the large, long-lived magnetic-fluctuation events whose amplitudes for $\delta = \pi/2$ and $\delta = -\pi/2$ peak at ~ 23.5 and ~ 22.5 ms, respectively, in Fig. 3. The associated

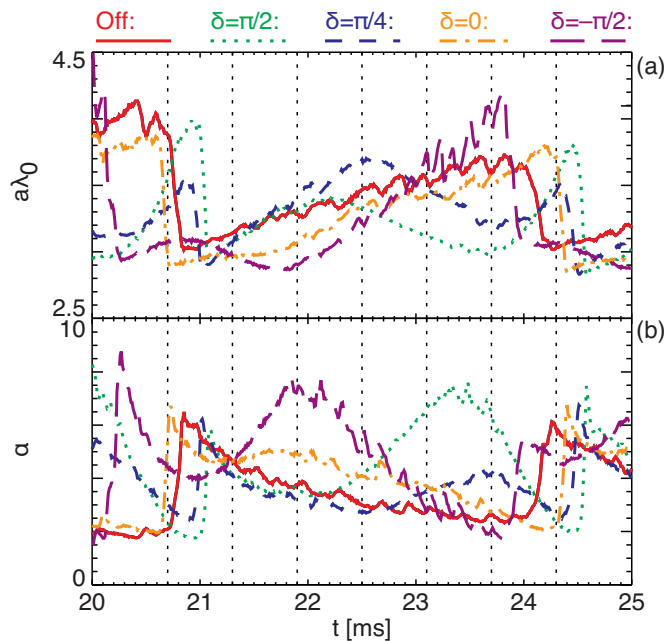


FIG. 4. (Color online) Time dependences including a single OFCD period of equilibrium quantities from the relaxed-state model for individual pulses representative of the ensembles. The core normalized parallel current $a\lambda_0$ (a) and the profile flatness parameter α (b) are shown for OFCD off (red solid) and OFCD on at $\delta = \pi/2$ (green dotted), $\delta = \pi/4$ (blue dashed), $\delta = 0$ (orange dashed-dotted), and $\delta = -\pi/2$ (purple long-dashed). Time points for equilibrium reconstructions are indicated by vertical dotted lines.

$m=0$ excursions can be especially large, for individual pulses exceeding 100 G in magnitude and lasting for longer times than the averages shown here. This activity in relation to the equilibrium evolution is discussed further below.

Since the time resolution for the full equilibrium reconstructions is insufficient to examine entrained sawteeth for OFCD cases in detail, and since pulse averaging for the OFCD-off case removes undulatory components due to the sawtooth relaxation cycle, representative single pulses chosen from each ensemble are compared using the relaxed-state model. This analysis provides time dependences of equilibrium profiles including the core normalized parallel-current density λ_0 and the λ -profile flatness parameter α , which are shown in Fig. 4. The chosen pulse for the OFCD-off pulse has two sawtooth events at about the same times as the entrained sawteeth for the OFCD pulses. For the OFCD cases $\delta = \pi/4$ and $\delta = 0$ the overall sawtooth-cycle effect on the λ profile is about the same as or larger than the OFCD effect, while for $\delta = \pi/2$ and $\delta = -\pi/2$ roughly the opposite is true, with large changes in α correlated with the intersawtooth events. Not shown in the figure are the core values q_0 of the safety factor $q = rB_\phi / (RB_\theta)$, for which OFCD modulations are about the same in size as changes due to sawteeth, and whose cycle averages are around $\langle q_0 \rangle \approx 0.2$.

The intersawtooth magnetic-fluctuation events tend to occur with relatively flat λ profiles (unlike sawtooth events which are triggered during peaked profiles). They correlate with large values of the edge parallel electric field and outward motion of the plasma, as shown in Fig. 5, a comparison of the ensembles for $\delta = \pi/2$ and $\delta = \pi/4$. The applied OFCD modulates both the edge parallel electric field $E_{||}(a)$

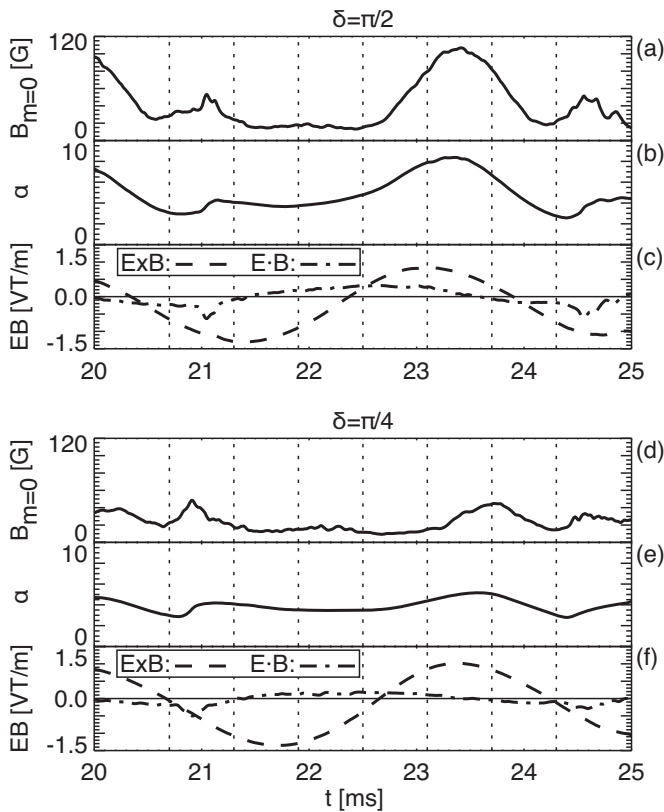


FIG. 5. Time dependences including a single OFCD period of the $m=0$ ($1 \leq n \leq 4$) mode magnetic-fluctuation amplitude (a), the profile flatness parameter α (b), and the products of edge equilibrium electric and magnetic fields (c) $[\mathbf{E}(a) \times \mathbf{B}(a)]_r$ (dashed) and $\mathbf{E}(a) \cdot \mathbf{B}(a)$ (dashed-dotted) for the $\delta = \pi/2$ ensemble (top), with the same quantities [(d)–(f)] for the $\delta = \pi/4$ ensemble (bottom). Time points for equilibrium reconstructions are indicated by vertical dotted lines.

[indicated in the plot by $\mathbf{E}(a) \cdot \mathbf{B}(a)$, with $B \approx 0.1$ T], and $[\mathbf{E}(a) \times \mathbf{B}(a)]_r$, which is indicative of plasma radial-pinch flow velocity. In the $\delta = \pi/2$ case, $E_{\parallel}(a)$ peaks in the codriving direction at ~ 22.5 ms, just as $[\mathbf{E}(a) \times \mathbf{B}(a)]_r$ is starting its outward excursion. At about the same time the λ profile is becoming flatter, i.e., α is increasing, and then the $m=0$ magnetic-fluctuation amplitude increases sharply, peaking as does α at ~ 23.5 ms. After this both the $m=0$ signal and α quickly decrease, reaching their minima with a more peaked λ profile a little after 24 ms. Meanwhile $E_{\parallel}(a)$ has become antidrive and outward pinch flow has ceased, just as the entrained sawtooth event is about to occur. In the $\delta = \pi/4$ case this progression is significantly muted, with lower peaks in $E_{\parallel}(a)$, α , and the $m=0$, as well as different phasings between $E_{\parallel}(a)$ and $[\mathbf{E}(a) \times \mathbf{B}(a)]_r$. The remaining OFCD phases are not shown in Fig. 5, but for $\delta = 0$ there is even less intersawtooth activity, and for $\delta = -\pi/2$ it comes up again, with different (and earlier) timings than for $\delta = \pi/2$. Similar $m=0$ activity can occur in nonoptimized inductive current-profile control experiments when the applied $E_{\parallel}(a)$ is made larger than needed to suppress fluctuations.³¹

Perhaps this intersawtooth activity corresponds to linear instability of edge-resonant $m=0$ modes, unlike RFP sawtooth activity, where the $m=0$ are nonlinearly driven by core-resonant $m=1$ modes.³⁰ The $m=0$ are typically linearly

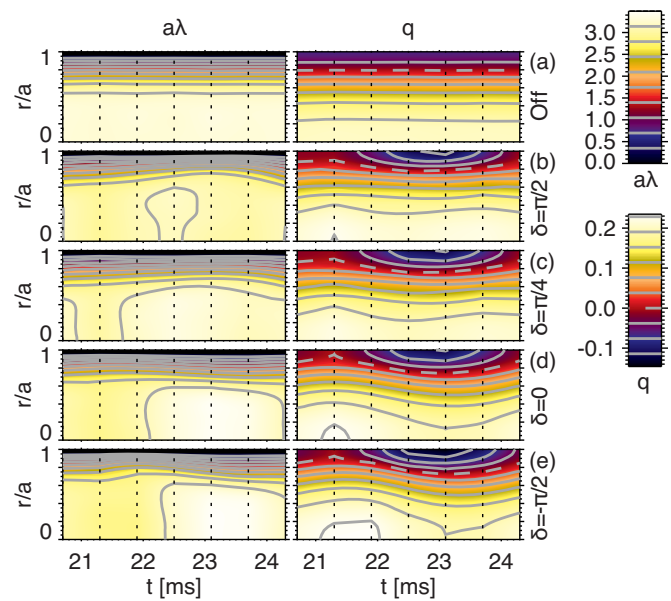


FIG. 6. (Color online) Time dependences over a single OFCD period of radial profiles of normalized parallel current $a\lambda$ (left) and safety factor q (right) for pulse ensembles with OFCD off (a) and OFCD on at $\delta = \pi/2$ (b), $\delta = \pi/4$ (c), $\delta = 0$ (d), and $\delta = -\pi/2$ (e). Time points for equilibrium reconstructions are represented as the left and right plot boundaries and the vertical dotted lines.

stable in a RFP with a sufficiently close-fitting conducting shell like MST's.³² However, during OFCD the $q=0$ resonant surface is modulated inward and outward as the λ profile varies, and this may periodically lessen the stabilizing effect of the shell. The modulation is shown for the full ensemble equilibrium reconstructions in Fig. 6, which agree with the relaxed-state modeling used above. The edge of the λ profile's plateau moves radially in and out for each OFCD phase, and this may periodically lessen the stabilizing effect of the shell. The modulation is shown for the full ensemble equilibrium reconstructions in Fig. 6, which agree with the relaxed-state modeling used above. The edge of the λ profile's plateau moves radially in and out for each OFCD phase, and this may periodically lessen the stabilizing effect of the shell. The modulation is shown for the full ensemble equilibrium reconstructions in Fig. 6, which agree with the relaxed-state modeling used above.

The time averages of these OFCD equilibrium profiles (not shown) are similar to, although slightly more flat than, those for OFCD off. The $q=0$ surfaces and edges of the λ -profiles for the OFCD cases are shifted radially outward by up to about 5% of r/a , and the core value of λ is decreased by about the same amount.

Reconstructions of the equilibrium magnetic-field profiles show that while the time-varying vector components in the edge region are mostly locked to the phase of their respective sources in OFCD, induced oscillations in the core of both the B_{ϕ} and B_{θ} profiles tend to follow the timing of the applied V_{ϕ} oscillation (which is changed to vary δ), as indicated in Fig. 7. This is consistent with a nearly force-free core plasma, satisfying $\nabla \times \mathbf{B} \approx \lambda \mathbf{B}$, with both components of \mathbf{B} tracking together in time. The amplitude of the ϕ component of the applied electric-field $\hat{E}_{\phi} \approx 3\hat{E}_{\theta}$ is larger than that of the θ component, which may select which source the two \mathbf{B} components in the core will track.

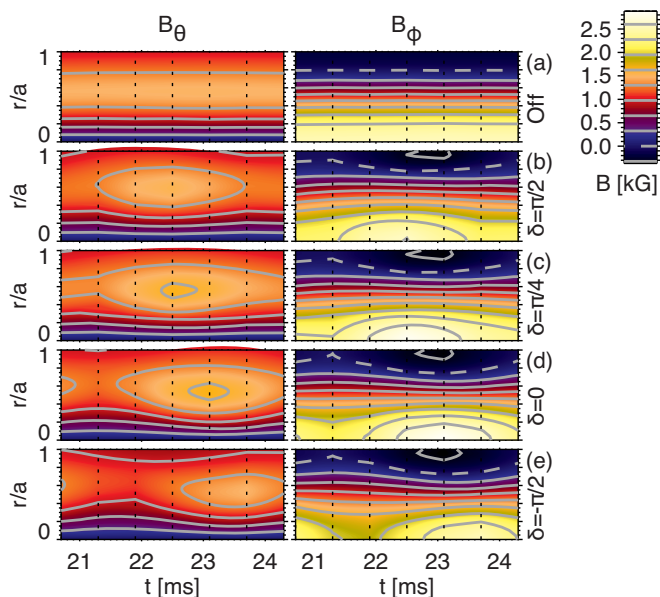


FIG. 7. (Color online) Time dependences over a single OFCD period of radial profiles of poloidal B_θ (left) and toroidal B_ϕ (right) magnetic field for pulse ensembles with OFCD off (a) and OFCD on at $\delta = \pi/2$ (b), $\delta = \pi/4$ (c), $\delta = 0$ (d), and $\delta = -\pi/2$ (e). Time points for equilibrium reconstructions are represented as the left and right plot boundaries and the vertical dotted lines.

C. Equilibrium electric-field evolution

Various aspects of equilibrium electric fields in OFCD are described in this section, starting with profiles of the vector components versus time. The cycle-average effective OFCD field is then defined and shown to be localized to the edge, and to vary with δ , as expected. Next the components of Ohm's law parallel to \mathbf{B} are shown, connecting both to the magnetic-fluctuation activity discussed above and to the energy and helicity balance discussed later. The perpendicular electric field, which appears to relate also to energy balance, is discussed last.

Radial profiles of the equilibrium inductive electric fields calculated from the reconstructions are shown in Fig. 8. For the OFCD cases an E_ϕ oscillation penetrates to the core with an amplitude attenuated to a few V/m, compared to about 10 V/m at the edge, resulting in negative core values during parts of the cycle. The edge E_θ , like its inductive counterpart B_ϕ , is roughly fixed in time by its fixed source as the edge E_ϕ source is moved later in time to decrease δ . Meanwhile the core (or midradius) E_θ phase moves later (again similar to the core B_ϕ) as the core E_ϕ phase moves earlier, oppositely to its source. This is similar to the entraining of sawteeth to the phase of E_θ relative to E_ϕ noted previously. Perhaps it implies a relationship between the penetration of E_ϕ and the entrained magnetic-relaxation activity.

OFCD should produce an effective electric field $\langle E \rangle_{\text{OFCD}} = \langle \mathbf{E} \cdot \mathbf{B} \rangle / \langle B \rangle - \langle E \rangle \cdot \langle \mathbf{B} \rangle / \langle B \rangle$, with brackets denoting cycle averages, localized to the edge of the plasma. The subtracted parallel average electric field $\langle E \rangle_{\parallel} = \langle \mathbf{E} \cdot \langle \mathbf{B} \rangle \rangle / \langle B \rangle$ would vanish in full OFCD. Radial profiles of both $\langle E \rangle_{\text{OFCD}}$ and $\langle E \rangle_{\parallel}$ are shown in Fig. 9 for the different ensembles. For the OFCD-off case $\langle E \rangle_{\text{OFCD}}$ vanishes as expected and for the

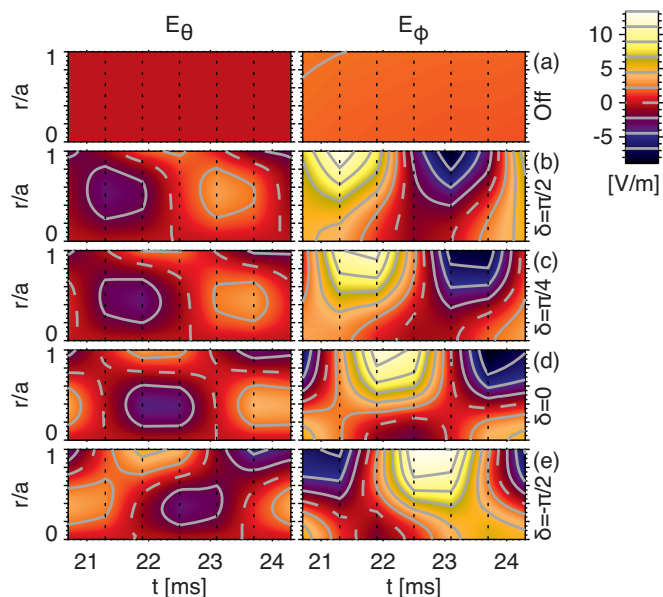


FIG. 8. (Color online) Time dependences over a single OFCD period of radial profiles of poloidal E_θ (left) and toroidal E_ϕ (right) electric field for pulse ensembles with OFCD off (a) and OFCD on at $\delta = \pi/2$ (b), $\delta = \pi/4$ (c), $\delta = 0$ (d), and $\delta = -\pi/2$ (e). Time points for equilibrium reconstructions are represented as the left and right plot boundaries and the vertical dotted lines.

OFCD cases it tracks with the respective OFCD helicity-injection rates ($\propto \sin \delta$) at the edge and falls to zero at $r/a \approx 0.5$, as seen in Fig. 9(a). As seen in Fig. 9(b), the $\langle E \rangle_{\parallel}$ field is not identical for all the ensembles, but varies in accordance with the cycle average $\langle V_\phi \rangle$ which is smallest for $\delta = \pi/4$, connoting a lower plasma resistance in that case.

OFCD also changes the behavior of the fluctuation-induced EMF \mathcal{E}_{\parallel} in the parallel Ohm's law $E_{\parallel} + \mathcal{E}_{\parallel} = \eta J_{\parallel}$. For a RFP sustained solely by toroidal induction this dynamolike term is responsible for maintenance of the current profile although $E_{\parallel} = \mathbf{E} \cdot \mathbf{B} / B$ and $\eta J_{\parallel} = \eta \mathbf{J} \cdot \mathbf{B} / B$ are unequal everywhere except at one radius.³⁰ It is often taken to be an ensemble average $\mathcal{E}_{\parallel} = \{ \tilde{\mathbf{U}} \times \tilde{\mathbf{B}} \}_{\parallel} - \{ (1/en) \tilde{\mathbf{J}} \times \tilde{\mathbf{B}} \}_{\parallel}$, where both a

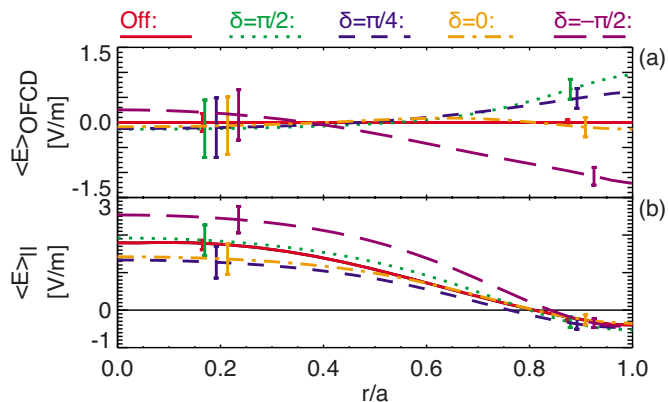


FIG. 9. (Color online) Radial profiles of effective OFCD electric field $\langle E \rangle_{\text{OFCD}} = \langle \mathbf{E} \cdot \mathbf{B} \rangle / \langle B \rangle - \langle E \rangle_{\parallel}$ (a) and parallel time-average electric field $\langle E \rangle_{\parallel} = \langle \mathbf{E} \cdot \langle \mathbf{B} \rangle \rangle / \langle B \rangle$ (b) for pulse ensembles with OFCD off (red solid) and OFCD on at $\delta = \pi/2$ (green dotted), $\delta = \pi/4$ (blue dashed), $\delta = 0$ (orange dashed-dotted), and $\delta = -\pi/2$ (purple long-dashed). Uncertainty estimates are shown at core and edge radii.

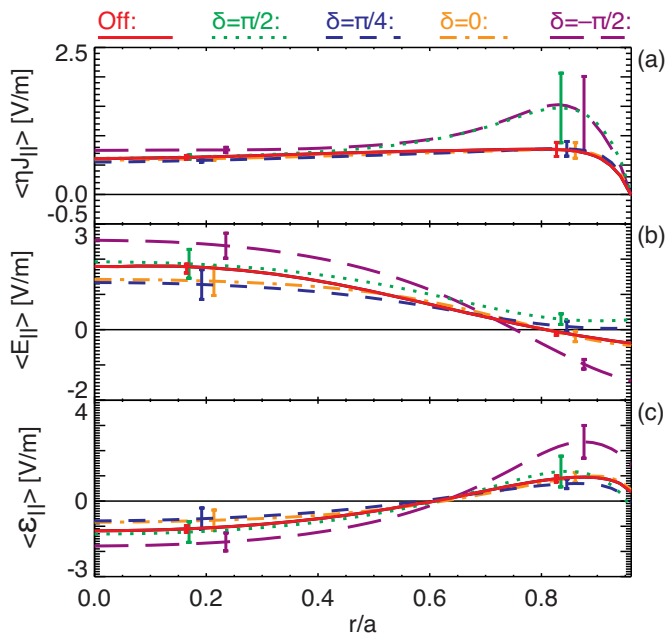


FIG. 10. (Color online) Radial profiles out to the limiter of cycle-average quantities in a parallel Ohm's law for pulse ensembles. The resistive term $\langle \eta J_{\parallel} \rangle$ (a), the electric field $\langle E_{\parallel} \rangle$ (b), and the EMF $\langle \mathcal{E}_{\parallel} \rangle = \langle \eta J_{\parallel} - E_{\parallel} \rangle$ (c) are shown for OFCD off (red solid) and OFCD on at $\delta = \pi/2$ (green dotted), $\delta = \pi/4$ (blue dashed), $\delta = 0$ (orange dashed-dotted), and $\delta = -\pi/2$ (purple long-dashed). Uncertainty estimates are shown at core and edge radii.

plasma-flow fluctuation \tilde{U} (Refs. 33 and 34) and a plasma-current fluctuation \tilde{J} (Ref. 35) interacting with the magnetic-field fluctuation \tilde{B} have been found to be important in previous RFP experiments. The equilibrium reconstructions used here are insensitive to the mechanism, and give just a measurement of the total EMF $\mathcal{E}_{\parallel} = \eta J_{\parallel} - E_{\parallel} = \mathcal{E} \cdot \mathbf{B} / B$.²⁷ A positive \mathcal{E}_{\parallel} corresponds to fluctuation-induced electromotive current drive and to inward transport of magnetic helicity,^{36,37} and vice versa for $\mathcal{E}_{\parallel} < 0$. The cycle averages $\langle \eta J_{\parallel} \rangle$, $\langle E_{\parallel} \rangle$, and $\langle \mathcal{E}_{\parallel} \rangle$ are shown in Fig. 10 for the different ensembles.

The $\delta = \pi/4$ case is found to roughly zero the cycle average $\langle \mathcal{E}_{\parallel} \rangle$ at the very edge of the plasma, in that the net OFCD current drive counters the antidrive supplied by the background toroidal induction, as shown in Fig. 10(c). This is accompanied by a slightly smaller $\langle \mathcal{E}_{\parallel} \rangle$ than the other cases, in particular, the OFCD-off case, at most radii. That this is true in the edge plasma seems consistent with observed lower levels of $m=0$ modes, but the slightly smaller levels of $\langle \mathcal{E}_{\parallel} \rangle$ for $\delta = \pi/4$ and $\delta = 0$ in the core might also seem to imply smaller $m=1$ levels than for the OFCD-off case as well, which are not observed. The $\langle \eta J_{\parallel} \rangle$ profiles for $\delta = \pi/2$ and $\delta = -\pi/2$ are significantly hollower than the others due mostly to their intersawtooth η -profile excursions (not shown). Note that $\langle E_{\parallel} \rangle = \langle \mathbf{E} \cdot \mathbf{B} / B \rangle$, an average weighted by instantaneous projection along \mathbf{B} / B , is similar in principle but not identical to $\langle E_{\parallel} \rangle = \langle \mathbf{E} \cdot \langle \mathbf{B} \rangle / \langle B \rangle \rangle$, the average projected along an average direction $\langle \mathbf{B} \rangle / \langle B \rangle$. They differ noticeably in the edge, where \mathbf{B} changes direction significantly during a cycle, as may be seen in comparing Figs. 10(b) and 9(b).

For the different ensembles the terms in $E_{\parallel} + \mathcal{E}_{\parallel} = \eta J_{\parallel}$ are shown in radial profile versus time in Fig. 11. Here it is seen

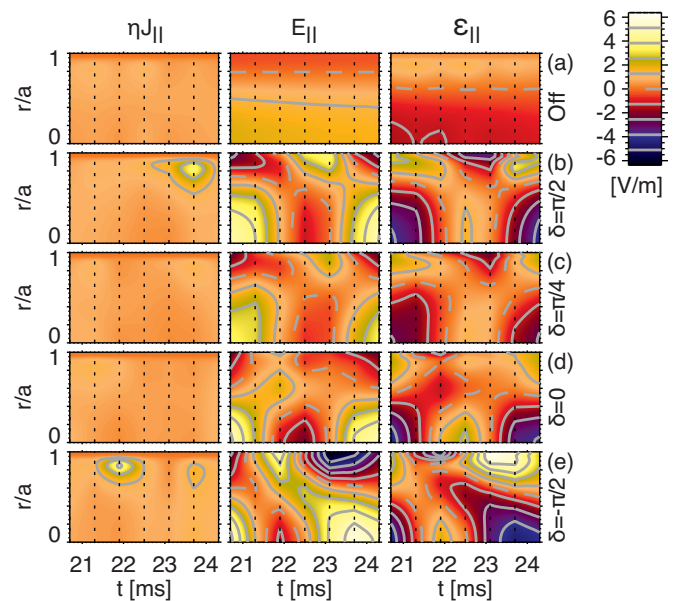


FIG. 11. (Color online) Time dependences over a single OFCD period of radial profiles of quantities in a parallel Ohm's law for pulse ensembles. The resistive term ηJ_{\parallel} (left), the electric field E_{\parallel} (middle), and the EMF $\mathcal{E}_{\parallel} = \eta J_{\parallel} - E_{\parallel}$ (right) are shown for OFCD off (a) and OFCD on at $\delta = \pi/2$ (b), $\delta = \pi/4$ (c), $\delta = 0$ (d), and $\delta = -\pi/2$ (e). Time points for equilibrium reconstructions are represented as the left and right plot boundaries and the vertical dotted lines.

that the oscillations in E_{\parallel} are mostly responsible for those in the \mathcal{E}_{\parallel} profile during OFCD, being generally much larger than the ηJ_{\parallel} profiles. Between the entrained sawteeth each of the OFCD cases has a period of positive \mathcal{E}_{\parallel} in the core, which would not occur there without OFCD. This transitions into a time of negative core \mathcal{E}_{\parallel} , typical of the RFP sustained by toroidal induction alone, and corresponding to the entrained sawtooth and large (core-resonant) $m=1$ mode activity. Note that the $\delta = \pi/4$ and $\delta = 0$ cases show smaller \mathcal{E}_{\parallel} oscillations at the edge than do $\delta = \pi/2$ and $\delta = -\pi/2$, which seems to comport with their lower level of edge-resonant $m=0$ activity. Also note the large positive excursions in the edge ηJ_{\parallel} at 23.7 ms for $\delta = \pi/2$ and at 21.9 ms for $\delta = -\pi/2$, each of which corresponds to a large positive edge excursion in E_{\parallel} and to an intersawtooth fluctuation event. Both of these ηJ_{\parallel} features are due more to η -profile excursions than to J_{\parallel} -profile excursions, although both are present. The large core and edge E_{\parallel} excursions at ~ 23.1 – 23.7 ms for $\delta = -\pi/2$ correspond to the entrained sawtooth.

According to a simple perpendicular Ohm's law, the applied oscillating \mathbf{E}_{\perp} normal to \mathbf{B} and tangent to the flux surface generates an oscillating equilibrium radial-pinch flow of the plasma $\mathbf{U}_r = (\mathbf{E}_{\perp} - \eta \mathbf{J}_{\perp}) \times \mathbf{B} / B^2$, where the $\eta \mathbf{J}_{\perp}$ term is on the order of 1% of $|\mathbf{E}_{\perp}|$. In each OFCD case there is an oscillation in this \mathbf{U}_r of amplitude ~ 100 m/s atop a cycle-average inward pinch due to the background steady toroidal induction of ~ 20 m/s, as seen in Fig. 12. In similar plasmas the measured speed of outward diffusive particle transport³⁸ is of the same order, and so the extent to which this \mathbf{U}_r reflects actual plasma motion is not established. The calculated \mathbf{U}_r values are significant from the edge in to $r/a \approx 0.5$ for all OFCD phases and stagnate near the magnetic axis.

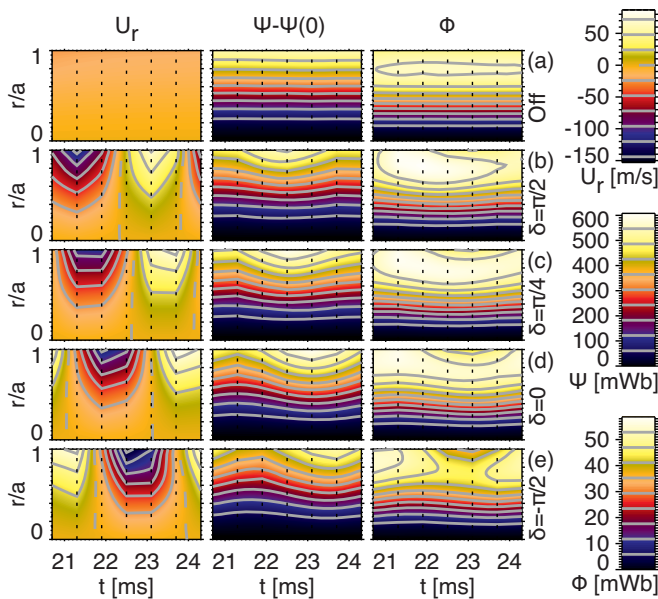


FIG. 12. (Color online) Time dependences over a single OFCD period of radial profiles of radial-pinch flow velocity U_r (left), enclosed poloidal magnetic flux $\Psi - \Psi(0)$ (middle), and toroidal magnetic flux Φ (right) for pulse ensembles with OFCD off (a) and OFCD on at $\delta = \pi/2$ (b), $\delta = \pi/4$ (c), $\delta = 0$ (d), and $\delta = -\pi/2$ (e). Time points for equilibrium reconstructions are represented as the left and right plot boundaries and the vertical dotted lines.

Also shown in Fig. 12 are surfaces of enclosed poloidal magnetic flux $\Psi - \Psi(0)$, whose oscillating motions are similar to those inferred of the plasma but which do not reflect the inward plasma pinch from the background induction, and of toroidal magnetic flux Φ . In the absence of diffusion or resistance magnetic flux surfaces would track with the radial positions of plasma elements.

D. Energy balance

The energy balance in OFCD experiments involves the cyclic evolution of the energy content and power flows, discussed first in this section, and the cycle-average thermal confinement properties, discussed last. As context, during a single sawtooth relaxation cycle in a standard RFP pulse without OFCD, both n_e and T_e in the core region drop during the sawtooth event, so that each of these quantities is effectively modulated around its mean by roughly 15% in relative amplitude. As the individual sawtooth times are different for each standard RFP pulse, these signals are mostly filtered out by ensemble averaging in this analysis. For OFCD cases the modulation amplitudes are about the same for n_e , but for the $\delta = \pi/4$ and $\delta = 0$ the relative T_e modulation amplitudes are about 30%, leading to $\sim 50\%$ electron-pressure modulations ($p_e \propto n_e T_e$) associated with the OFCD cycle itself rather than the entrained sawtooth. This is seen in Fig. 13, which shows radial profiles of the total fitted thermal-energy density $w_{th} = (3/2)p$ from equilibrium reconstructions (where $p \equiv 2p_e$), along with profiles of the magnetic-energy density $w_{mag} = B^2/(2\mu_0)$. In each OFCD case the n_e and T_e profiles (not shown) oscillate in phase with each other.

At the peak times the w_{th} profiles are rather flat out to $r/a \approx 0.5$. The different phases show drops in w_{th} around the

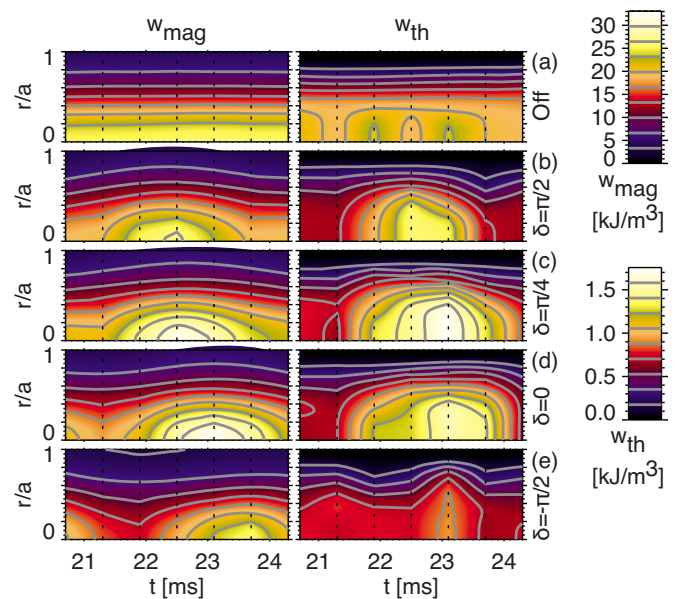


FIG. 13. (Color online) Time dependences over a single OFCD period of radial profiles of the magnetic w_{mag} (left) and thermal $w_{th} \equiv 2w_{th,e}$ (right) energy densities for pulse ensembles with OFCD off (a) and OFCD on at $\delta = \pi/2$ (b), $\delta = \pi/4$ (c), $\delta = 0$ (d), and $\delta = -\pi/2$ (e). Time points for equilibrium reconstructions are represented as the left and right plot boundaries and the vertical dotted lines.

times of sawteeth, while the peak times move roughly in phase with the applied V_ϕ (as do those for w_{mag}), with the exception of $\delta = -\pi/2$ which has a relatively small and incoherent w_{th} . Also note that the w_{th} peaks for $\delta = \pi/2$ and $\delta = -\pi/2$ are seriously degraded near the times of their intersawtooth events, ~ 23.7 and ~ 21.9 ms, respectively. The OFCD-off case shows some statistical w_{th} noise in the core due mostly to sawtooth activity remaining after ensemble averaging of data from individual pulses. On time average the OFCD w_{th} and w_{mag} profiles for $\delta = \pi/4$ and $\delta = 0$ are calculated to be slightly larger than that for OFCD off while those for $\delta = \pi/2$ and $\delta = -\pi/2$ are smaller.

Oscillating radial equilibrium motion due to OFCD might be expected to cause wall interactions that degrade plasma quality through repetitive refueling by cold particles of edge flux surfaces that periodically touch the wall.³⁹ The present results imply that such an effect is not a main factor in these experiments. As seen in comparing Figs. 12 and 13 for the different OFCD cases, inward radial motions of the plasma or flux surfaces are concurrent with periodic increases in edge w_{th} (and n_e and T_e) rather than decreases, and the edge thermal profiles for OFCD cases are similar to those for the OFCD-off case at the times of inward motions. Perhaps wall interactions become more important for OFCD at higher input powers or oscillation frequencies.

The calculated mechanical work due to oscillating equilibrium quantities shows qualitative agreement with the observed pressure oscillations in OFCD, as shown in Fig. 14. Here are time-dependent profiles of the respective terms in a (lossless) plasma heat equation $w'_{th} = -(5/2)p \nabla \cdot \mathbf{U} - (3/2)\mathbf{U} \cdot \nabla p + \eta J^2$,⁴⁰ in which w'_{th} , the rate of change of thermal-energy density at a point in space, that is the sum of two mechanical-power densities and the Ohmic-heating den-

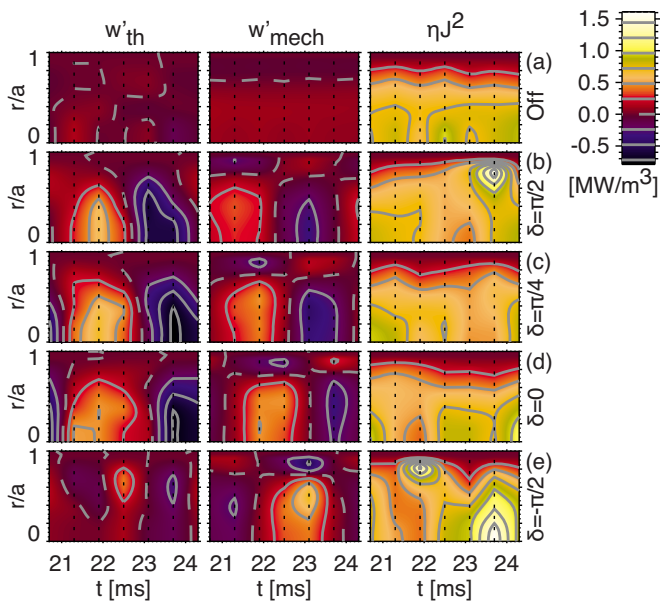


FIG. 14. (Color online) Time dependences over a single OFCD period of radial profiles of the rate of change of thermal-energy density $w'_{th} \equiv 2w'_{th,e}$ (left), the mechanical-power density $w'_{mech} = -(5/2)p \nabla \cdot \mathbf{U} - (3/2)\mathbf{U} \cdot \nabla p$ (middle), and the Ohmic-heating density ηJ^2 (right) for pulse ensembles with OFCD off (a) and OFCD on at $\delta = \pi/2$ (b), $\delta = \pi/4$ (c), $\delta = 0$ (d), and $\delta = -\pi/2$ (e). Time points for equilibrium reconstructions are represented as the left and right plot boundaries and the vertical dotted lines.

sity ηJ^2 . The total mechanical-power density $w'_{mech} = -(5/2)p \nabla \cdot \mathbf{U} - (3/2)\mathbf{U} \cdot \nabla p$, which includes the calculated equilibrium pinch effect, generally agrees temporally and roughly in magnitude with w'_{th} for the OFCD phases (other than $\delta = \pi/2$), with the compression term $-(5/2)p \nabla \cdot \mathbf{U}$ larger in the core and the convection term $-(3/2)\mathbf{U} \cdot \nabla p$ larger in the edge. The oscillating parts of the ηJ^2 profiles (not isolated in the figure) are generally weaker than the w'_{mech} terms and, when added to them, do not unambiguously affect the agreement with the w'_{th} terms. The steady parts of the ηJ^2 profiles dominate both w'_{mech} and w'_{th} , and therefore so do those of the transport losses. Other than general increases near sawteeth at the edges of the experimental time window and the sharp edge increases with the intersawtooth events at ~ 23.7 and ~ 21.9 ms for $\delta = \pi/2$ and $\delta = -\pi/2$, respectively, the OFCD ηJ^2 profiles lack a clear, modulated pattern as δ is varied.

The global energy-confinement properties calculated from these electron thermal measurements for the OFCD cases $\delta = \pi/4$ and $\delta = 0$ are slightly improved compared to those for the OFCD-off case, as shown in Fig. 15. Here the phase dependence for several quantities from spatially integrated cycle-averages are plotted: the energy-confinement time $\tau_E \equiv \langle W_{th} \rangle / \langle P_{th} - W'_{th} \rangle$, the normalized spatially averaged plasma thermal pressure $\beta \equiv 2\mu_0 \langle \bar{p} \rangle / \langle B^2(a) \rangle$, the total thermal energy $\langle W_{th} \rangle$, the total magnetic energy $\langle W_{mag} \rangle$, the total thermal input power $\langle P_{th} \rangle = \int_V \langle \eta J^2 - \mathbf{U} \times \mathbf{B} \cdot \mathbf{J} \rangle dv$, which is the volume integral of the heat equation above and which dominates W'_{th} in the denominator of τ_E , the total power transfer from the magnetic field $\int_V \langle \mathbf{E} \cdot \mathbf{J} \rangle dv$, and the total input power, or surface Poynting flux from the power supplies, $\langle P_{in} \rangle$. Note that the first three of these depend on ther-

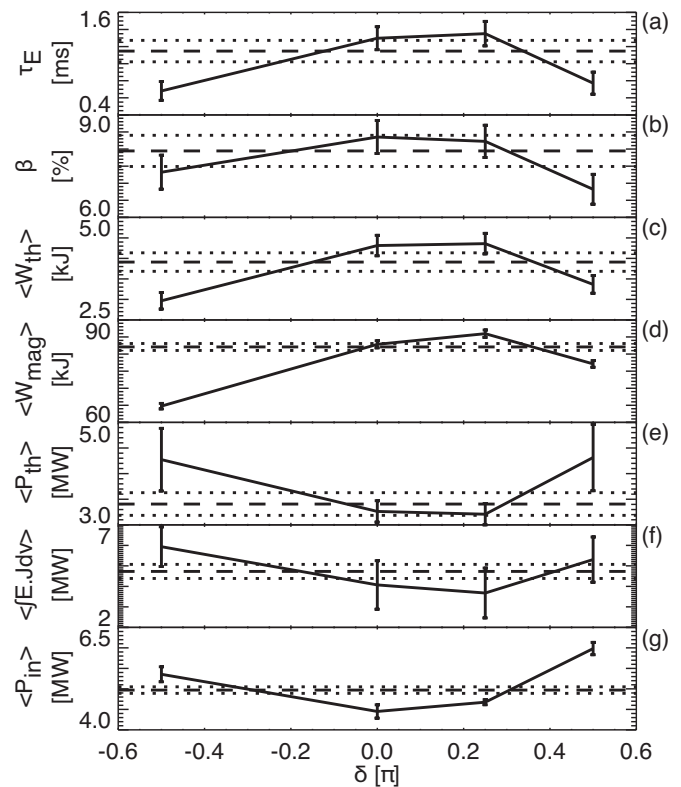


FIG. 15. Phase dependences of cycle-average global confinement quantities. The energy-confinement time $\tau_E \equiv \langle W_{th} \rangle / \langle P_{th} - W'_{th} \rangle$ (a), normalized spatially averaged plasma thermal pressure $\beta \equiv 2\mu_0 \langle \bar{p} \rangle / \langle B^2(a) \rangle$ (b), thermal energy $\langle W_{th} \rangle$ (c), magnetic energy $\langle W_{mag} \rangle$ (d), thermal input power $\langle P_{th} \rangle = \int_V \langle \eta J^2 - \mathbf{U} \times \mathbf{B} \cdot \mathbf{J} \rangle dv$ (e), power transfer from the magnetic field $\int_V \langle \mathbf{E} \cdot \mathbf{J} \rangle dv$ (f), and input power $\langle P_{in} \rangle$ (g) are shown for OFCD ensembles (solid) and the OFCD-off ensemble (dashed with dotted uncertainties).

mal pressure and are scaled electron thermal quantities, assuming the ion pressure p_i , which was not measured for this work, equals the electron pressure p_e , which is approximately the case in previous OFCD experiments. Ion heat is mainly sourced by reconnection from fluctuations due to equilibrium instabilities, and is practically decoupled from electron heat in these plasmas due to relatively long times of equilibration between them. The main loss channel for both electron and ion energy is through magnetic fluctuations and their respective confinement times are estimated to be similar in plasmas such as the baseline RFPs used here.⁴¹

Compared to the OFCD-off case, the OFCD cases $\delta = \pi/4$ and $\delta = 0$ show slightly higher τ_E (≈ 1 ms), β ($\approx 8\%$), $\langle W_{th} \rangle$, and $\langle W_{mag} \rangle$, and slightly lower $\langle P_{th} \rangle$, $\int_V \langle \mathbf{E} \cdot \mathbf{J} \rangle dv$, and $\langle P_{in} \rangle$, with differences around the levels of the measurement uncertainties. The other OFCD cases, $\delta = \pi/2$ and $\delta = -\pi/2$, compare oppositely to the OFCD-off case and tend to have larger differences from it. These phase dependences are consistent with previous, less thorough, experimental findings¹⁰ but note that they could be changed if ion heating and energy content were specifically included in the values. For instance, the actual $\beta \equiv 2\mu_0 \langle \bar{p}_e + \bar{p}_i \rangle / \langle B^2(a) \rangle$ may be flatter than shown in Fig. 15 as ion heating due to magnetic fluctuations is expected to be larger for $\delta = \pi/2$ and $\delta = -\pi/2$ and smaller for $\delta = \pi/4$ and $\delta = 0$.

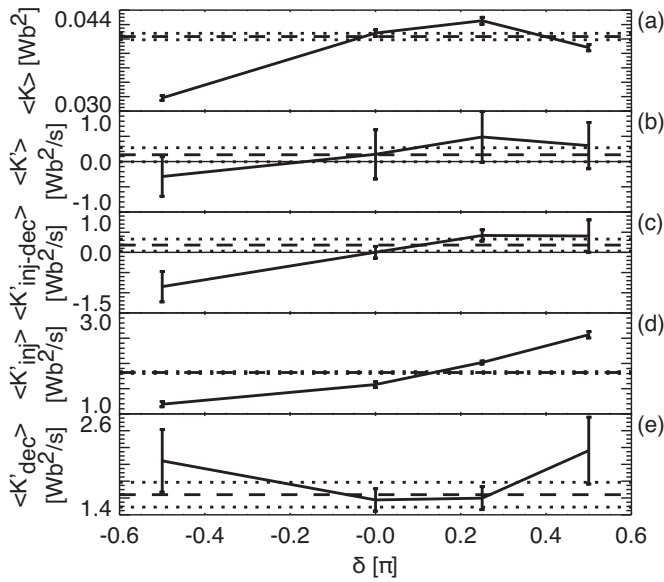


FIG. 16. Phase dependences of cycle-average global quantities in the helicity balance. The helicity content $\langle \mathcal{K} \rangle = 2 \langle \int_{\psi} \Phi d\Psi \rangle$ (a), its rate of change $\langle \mathcal{K}' \rangle$ (b), the injection minus decay rate $\langle \mathcal{K}'_{inj-dec} \rangle = 2 \langle V_{\phi} \Phi \rangle$ (c), the injection rate $\langle \mathcal{K}'_{inj} \rangle = 2 \langle V_{\phi} \Phi \rangle$ (d), and the decay rate $\langle \mathcal{K}'_{dec} \rangle = 2 \langle \eta \mathbf{J} \cdot \mathbf{B} \rangle$ (e) are shown for OFCD ensembles (solid) and the OFCD-off ensemble (dashed with dotted uncertainties).

E. Helicity balance

The helicity balance may help explain the observed OFCD phase dependence of the added plasma current. The rate of change of global helicity content $\mathcal{K}' = 2V_{\phi}\Phi - 2\int \eta \mathbf{J} \cdot \mathbf{B} dv$, which is the difference of an injection rate and a decay rate, is generally well balanced with the measured quantities at each time for the various ensembles, and on cycle average, which is shown in Fig. 16. The cycle averages of the total helicity content $\langle \mathcal{K} \rangle = 2 \langle \int_{\psi} \Phi d\Psi \rangle$, its rate of change $\langle \mathcal{K}' \rangle$, the measured injection minus decay rate, the injection rate $\langle \mathcal{K}'_{inj} \rangle = 2 \langle V_{\phi} \Phi \rangle$, and the decay rate $\langle \mathcal{K}'_{dec} \rangle = 2 \langle \eta \mathbf{J} \cdot \mathbf{B} \rangle$ for the OFCD cases are compared to those for the OFCD-off case. The measured averages $\langle \mathcal{K}' \rangle$ and $\langle \mathcal{K}'_{inj} \rangle - \langle \mathcal{K}'_{dec} \rangle$, both of which are much smaller than their oscillation levels (not shown), agree well for all phases, with the exception of $\delta = -\pi/2$, whose relatively poor agreement seems to be due to entrained sawtooth pollution at 23.7 ms.

As seen in Fig. 16(e), the cycle-average decay rates $\langle \mathcal{K}'_{dec} \rangle$ are minimal for the OFCD phases $\delta = 0$ and $\delta = \pi/4$, for which the calculated values are essentially the same as in the OFCD-off case. Conversely for $\delta = \pi/2$ and $\delta = -\pi/2$ the decay rates are measured to be larger than for the OFCD-off case. The differences in decay rates for the different cases are mostly due to their η , as opposed to their $\mathbf{J} \cdot \mathbf{B}$, profiles. For $\delta = \pi/2$, the relatively high decay rate, largely due to the intersawtooth event, helps to explain the observation that its added plasma current I_{ϕ} (related to \mathcal{K}) tends to be relatively small or zero.¹⁰ However, with large uncertainty estimates, the observed $\langle \mathcal{K}' \rangle \approx 2 \langle V_{\phi} \Phi - \int \eta \mathbf{J} \cdot \mathbf{B} dv \rangle$ [Figs. 16(b) and 16(c)] for $\delta = \pi/2$ and $\delta = \pi/4$ are similar, despite that the added I_{ϕ} tends to be significantly larger for the $\delta = \pi/4$ case. The respective $\langle \mathcal{K} \rangle$ values do comport with the I_{ϕ} observations, and this single-cycle $\langle \mathcal{K}' \rangle$ comparison does not take

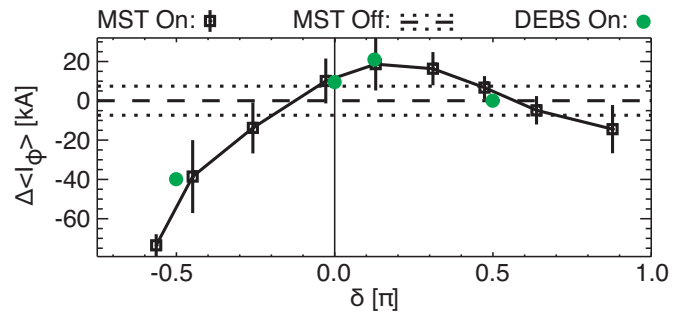


FIG. 17. (Color online) Phase dependence of the change in cycle-average plasma current $\Delta \langle I_{\phi} \rangle$ for the OFCD experiments in Ref. 10 (squares) compared to the OFCD-off case (dashed with dotted uncertainties), with results from a numerical MHD simulation overlaid (green circles).

into account larger discrete events sometimes observed in earlier or later cycles, especially for the $\delta = \pi/2$ case, that result in sharp drops in I_{ϕ} , and presumably $\langle \mathcal{K}' \rangle$. Those events seem to be like the intersawtooth events described above.

V. NUMERICAL SIMULATIONS

Nonlinear numerical simulations of previous partial OFCD experiments¹⁰ were done using the 3D resistive-MHD code DEBS.⁴² The code was run with a Lunquist number of $S = 10^5$, similar to the estimated experimental value, and used time-dependent boundary conditions for the applied voltages close to those used in the experiments. Four OFCD runs were done, for the phases $\delta = \pi/2$, $\delta = \pi/8$, $\delta = 0$, and $\delta = -\pi/2$, and the resulting phase dependence of the resulting added plasma current $\Delta \langle I_{\phi} \rangle$ after several OFCD cycles is remarkably close to that observed in the experiments, as shown in Fig. 17.

The optimum case $\delta = \pi/8$ in the code exhibited a more quiescent λ profile over its cycle than did $\delta = \pi/2$ or $\delta = -\pi/2$, just as it did in the experiments, as did the nearby phases $\delta = \pi/4$ and $\delta = 0$ in the experiments reported here. The magnetic-fluctuation spectrum from the code did not agree closely with the experiments in all details, but did show a minimization of $m=1$ amplitudes for the case $\delta = \pi/8$, which is like the experimental result. The differences between code and experiment were clearer for the $m=0$ modes, probably due mostly to differences in how the boundary conditions are applied in the two cases. In the experiment the power-supply setting for the V_{θ} oscillation is chosen to maintain edge magnetic-field $B_{\phi}(a)$ reversal, with relatively more control over $B_{\phi}(a)$ than V_{θ} itself, which can be distorted by plasma activity such as sawteeth due to finite supply impedance. In the code V_{θ} is strictly the boundary condition, and the resulting equilibrium can go out of $B_{\phi}(a)$ reversal, as it did periodically for some of the phases in the simulations. This would remove the $m=0$ resonant surface from the plasma resulting in different overall results for $m=0$ activity.

A chief finding of the simulations was that the $\delta = \pi/2$ case has increased dissipation $2 \langle \eta \mathbf{J} \cdot \mathbf{B} \rangle$ practically canceling its maximal helicity injection, again similar to the experimental results above. However, in the code runs the as-

sumed S -dependent resistivity profile was the same for all phases, which means the higher dissipation for $\delta = \pi/2$ was due entirely to its $\mathbf{J} \cdot \mathbf{B}$ profile. This is different than the experimental result which has the η profile mostly determining $2\int \langle \eta \mathbf{J} \cdot \mathbf{B} \rangle dv$ versus δ .

Understanding this difference might be useful. Conceivably some of the agreement in Fig. 17 could be fortuitous; for example, the cycle-average plasma currents in the code were allowed to saturate to a steady value while those in the experiment were still increasing at the end of the applied OFCD. Still, the good qualitative agreement in phase dependences of $\Delta \langle I_\phi \rangle$ may suggest an underlying degree of self-organizing behavior not strongly dependent on details of energy transport or resistivity. Perhaps, for given OFCD amplitudes and phase, the $\langle \eta(r) \mathbf{J}(r) \cdot \mathbf{B}(r) \rangle$ profile adjusts through modulations and fluctuations to allow some acceptable rate of increase of helicity, by adjusting $\eta(r)$, $\mathbf{J}(r) \cdot \mathbf{B}(r)$, or both.

VI. CONCLUSION

The two main results of the experiments reported here, which are the small improvement in measured energy confinement for the phases $0 \leq \delta \leq \pi/4$ compared to the OFCD-off case and the relatively large helicity dissipation for $\delta = \pi/2$, are discussed. First, at $0 \leq \delta \leq \pi/4$ the applied OFCD tends toward minimizing the cycle-average EMF $\langle \mathcal{E}_\parallel \rangle$ and results in smaller $m=0$ magnetic fluctuations and the most quiescent OFCD profiles, with marginally better global confinement than the standard case. Net helicity dissipation is minimal, which is qualitatively consistent with the small (5%–10%) added current typically observed for $\delta \approx \pi/8$ despite the only small helicity injection added by OFCD. Note that the total helicity injection implied above (Fig. 16) for $\delta = \pi/8$ is nearly unchanged from the OFCD-off case; the OFCD adds some net positive injection $(\hat{V}_\phi \hat{V}_\theta / \omega) \sin \delta$ offset by a decrease in the background injection $2\langle V_\phi \rangle \langle \Phi \rangle$ from the small drop in net loop voltage $\langle V_\phi \rangle$. The total helicity dissipation implied above for $\delta = \pi/8$ is slightly decreased compared to that for the OFCD-off case.

Second, for $\delta = \pi/2$, the measured energy confinement is measurably degraded, and the helicity dissipation is maximized so as to mostly cancel the maximum OFCD helicity injection, leading to a relatively small added plasma current. In the experiments the decay effect is mostly due to increases in resistivity associated with discrete, intersawtooth magnetic-fluctuation events induced by the applied oscillations. These appear as large pulses in $m=0$ (and $m=1$) amplitude as the λ profile is outwardly extended once per cycle in tandem with a strong edge codriving parallel electric field. As they occur when the λ profile is relatively flat globally but steepened in the edge near the $q=0$ surface, they may be driven by linear $m=0$ instability, unlike the standard sawtooth activity. The intersawtooth events do not seem to be primarily a wall-interaction effect in that, although they occur as the plasma is inferred to be moving outward into the wall, they are not nearly as large for the $\delta = \pi/4$ and $\delta = 0$ cases, for which such outward motion is about the same, but which lack the strong edge cocurrent drive at the time.

Tests at higher OFCD powers (not discussed above) indicate similar magnetic-fluctuation events tend to occur even for these phases as the OFCD input power is increased.

Since the net OFCD injection rate is $(\hat{V}_\phi \hat{V}_\theta / \omega) \sin \delta$, a chosen rate at $\delta = \pi/2$ could be maintained with smaller voltage amplitudes (\hat{V}_ϕ , \hat{V}_θ , or both) if ω were also smaller to compensate, perhaps leading to smaller intersawtooth fluctuation events, lower dissipation, and therefore better current drive. The OFCD period $\tau = 1/\omega$ should satisfy $\tau_{\text{rel}} < \tau \ll \tau_{\text{res}}$, where τ_{res} is the resistive-diffusion time and $\tau_{\text{rel}} \sim (\tau_A \tau_{\text{res}})^{1/2}$ is the relaxation time, so that unidirectional plasma current is maintained while relaxation is allowed to distribute current into the core of the RFP.¹² For these MST plasmas, with $\tau_{\text{res}} \approx 500$ ms (and $\tau_{\text{rel}} \approx 0.1$ ms), an OFCD frequency slower than the present ($\tau \approx 0.5$ ms) could be satisfactory, with a lower limit defined by the minimum number of cycles experimentally useful during the MST pulse. Also, applying OFCD with waveforms that include higher harmonics might provide another way to mitigate or avoid large magnetic-fluctuation events while maintaining the same helicity-injection rate.

Note that the MST flattop and total OFCD duration to date have been less than about $L/R \approx 30$ ms in duration, which is the characteristic time over which added net plasma current would saturate exponentially by resistive diffusion. Therefore a longer flattop and OFCD pulse length would allow a larger added current at the optimum phase as saturation were approached, as well as a substantially lower ω .

Plans for future work include using upgraded, programmable power supplies on MST to extend both the RFP flattop and the OFCD pulse, and to better control the OFCD voltages (which presently are provided by tank circuits). Different frequencies, power levels, and waveforms can be tested at different plasma currents to possibly increase the added current while investigating limits to it. Programmable, real-time power-supply control would allow feedback to constant cycle-average current $\langle I_\phi \rangle$ while monitoring the change in net loop voltage $\langle V_\phi \rangle$, which occurs much more quickly than current saturation by resistive diffusion. Along with the internal diagnostics used for this paper and ion-temperature diagnostics for continued confinement tests and related studies, edge insertable probes will be used to study electromotive effects, with some preliminary work already done. Those experiments might also provide information on $m=0$ stability, along with further analysis of profiles already measured. Continued numerical MHD simulations would be useful for modeling OFCD scenarios with more realistic boundary conditions, to explore different parameter ranges including higher drive fractions, and to study thermal transport effects. In the longer term the S scaling of confinement in full OFCD is a key to RFP development and may be calculable for the range of possible future devices.

Summarizing, near the optimum phasing for added plasma current of up to about 10%, it is found that partial OFCD has slightly better energy confinement than that for the standard RFP without OFCD, based on electron thermal measurements in MST experiments. In contrast, at the phase of maximum helicity injection, for which the added current

is smaller, confinement is degraded, and helicity dissipation is increased mostly by increased resistance. These effects are ascribed to discrete magnetic-fluctuation events driven by the OFCD electric fields. Numerical MHD calculations modeling the experiments are consistent with them in the phase dependence of added current and in the general behavior of magnetic fluctuations. The question of confinement in OFCD remains for higher plasma-current fractions including the full-sustainment case, which is yet to be modeled numerically and which presently is beyond experimental capability.

ACKNOWLEDGMENTS

Paul Nonn is responsible for most of the design and construction of the OFCD hardware. We thank A. F. Almagri, B. E. Chapman, G. Fiksel, V. V. Mirnov, B. A. Nelson, S. C. Prager, D. D. Schnack, and J. C. Sprott for helpful conversations. This work was supported by the U.S. DOE Cooperative Agreement No. DE-FC02-05ER54814.

- ¹M. K. Bevir and J. W. Gray, in *Proceedings of the Reversed Field Pinch Theory Workshop* (LANL, Los Alamos, NM, 1981), Paper No. LA-8944-C, p. 176.
- ²H. A. B. Bodin and A. A. Newton, *Nucl. Fusion* **20**, 1255 (1980).
- ³A. H. Boozer, *Phys. Fluids* **31**, 591 (1988).
- ⁴J. S. Sarff, J. K. Anderson, T. M. Biewer, D. L. Brower, B. E. Chapman, P. K. Chattopadhyay, D. Craig, B. Deng, D. J. Den Hartog, W. X. Ding, G. Fixel, C. B. Forest, J. A. Goetz, R. O'Connell, S. C. Prager, and M. A. Thomas, *Plasma Phys. Controlled Fusion* **45**, A457 (2003).
- ⁵A. H. Boozer, *Phys. Fluids* **29**, 4123 (1986).
- ⁶K. F. Schoenberg, J. C. Ingraham, C. P. Munson, P. G. Weber, D. A. Baker, R. F. Gribble, R. B. Howell, G. Miller, W. A. Reass, A. E. Schofield, S. Shinohara, and G. A. Wurden, *Phys. Fluids* **31**, 2285 (1988).
- ⁷P. M. Bellan, *Nucl. Fusion* **29**, 78 (1989).
- ⁸S. Yamaguchi, M. J. Schaffer, and Y. Kondoh, *Fusion Eng. Des.* **26**, 121 (1995).
- ⁹R. N. Dexter, D. W. Kerst, T. W. Lovell, S. C. Prager, and J. C. Sprott, *Fusion Technol.* **19**, 131 (1991).
- ¹⁰K. J. McCollam, A. P. Blair, S. C. Prager, and J. S. Sarff, *Phys. Rev. Lett.* **96**, 035003 (2006).
- ¹¹F. Ebrahimi, S. C. Prager, J. S. Sarff, and J. C. Wright, *Phys. Plasmas* **10**, 999 (2003).
- ¹²H. R. Strauss and D. S. Harned, *Phys. Fluids* **30**, 164 (1987).
- ¹³D. S. Harned, D. D. Schnack, H. R. Strauss, and R. A. Nebel, *Phys. Fluids* **31**, 1979 (1988).
- ¹⁴P. M. Bellan, *Phys. Fluids* **27**, 2191 (1984).
- ¹⁵J. B. Taylor, *Phys. Rev. Lett.* **33**, 1139 (1974).
- ¹⁶J. Scheffel and D. D. Schnack, *Nucl. Fusion* **40**, 1885 (2000).
- ¹⁷F. Ebrahimi and S. C. Prager, *Phys. Plasmas* **11**, 2014 (2004).
- ¹⁸T. Bolzonella, P. Martin, S. Martini, L. Marrelli, R. Pasqualotto, and D. Terranova, *Phys. Rev. Lett.* **87**, 195001 (2001).

- ¹⁹D. Terranova, A. Alfier, F. Bonomo, P. Franz, P. Innocente, and R. Pasqualotto, *Phys. Rev. Lett.* **99**, 095001 (2007).
- ²⁰A. P. Blair, Ph.D. thesis, University of Wisconsin-Madison, 2006.
- ²¹Y. Jiang, D. L. Brower, and N. E. Lanier, *Rev. Sci. Instrum.* **70**, 703 (1999).
- ²²B. H. Deng, D. L. Brower, W. X. Ding, M. D. Wyman, B. E. Chapman, and J. S. Sarff, *Rev. Sci. Instrum.* **77**, 10F108 (2006).
- ²³D. J. Den Hartog, D. Craig, D. A. Ennis, G. Fiksel, S. Gangadhara, D. J. Holly, J. C. Reardon, V. I. Davydenko, A. A. Ivanov, A. A. Lizunov, M. G. O'Mullane, and H. P. Summers, *Rev. Sci. Instrum.* **77**, 10F122 (2006).
- ²⁴J. A. Reusch, M. T. Borchardt, D. J. Den Hartog, A. F. Falkowski, D. J. Holly, R. O'Connell, and H. D. Stephens, *Rev. Sci. Instrum.* **79**, 10E733 (2008).
- ²⁵J. K. Anderson, C. B. Forest, T. M. Biewer, J. S. Sarff, and J. C. Wright, *Nucl. Fusion* **44**, 162 (2004).
- ²⁶R. H. Good, *Eur. J. Phys.* **22**, 119 (2001).
- ²⁷J. K. Anderson, T. M. Biewer, C. B. Forest, R. O'Connell, S. C. Prager, and J. S. Sarff, *Phys. Plasmas* **11**, L9 (2004).
- ²⁸V. Antoni, P. Martin, and S. Ortolani, *Nucl. Fusion* **29**, 1759 (1989).
- ²⁹B. H. Deng, W. X. Ding, D. L. Brower, A. F. Almagri, K. J. McCollam, Y. Ren, S. C. Prager, J. S. Sarff, J. Reusch, and J. K. Anderson, *Plasma Phys. Controlled Fusion* **50**, 115013 (2008).
- ³⁰Y. L. Ho and G. G. Craddock, *Phys. Fluids B* **3**, 721 (1991).
- ³¹J. S. Sarff, A. F. Almagri, M. Cekic, C. S. Chaing, D. Craig, D. J. Den Hartog, G. Fiksel, S. A. Hokin, R. W. Harvey, H. Ji, C. Litwin, S. C. Prager, D. Sinitsyn, C. R. Sovinec, J. C. Sprott, and E. Uchimoto, *Phys. Plasmas* **2**, 2440 (1995).
- ³²Y. L. Ho and S. C. Prager, *Phys. Fluids* **31**, 1673 (1988).
- ³³D. J. Den Hartog, J. T. Chapman, D. Craig, G. Fiksel, P. W. Fontana, S. C. Prager, and J. S. Sarff, *Phys. Plasmas* **6**, 1813 (1999).
- ³⁴P. W. Fontana, D. J. Den Hartog, G. Fiksel, and S. C. Prager, *Phys. Rev. Lett.* **85**, 566 (2000).
- ³⁵W. X. Ding, D. L. Brower, D. Craig, B. H. Deng, G. Fiksel, V. Mirnov, S. C. Prager, J. S. Sarff, and V. Svidzinski, *Phys. Rev. Lett.* **93**, 045002 (2004).
- ³⁶H. Y. W. Tsui, *Nucl. Fusion* **28**, 1543 (1988).
- ³⁷H. Ji, *Phys. Rev. Lett.* **83**, 3198 (1999).
- ³⁸N. E. Lanier, D. Craig, J. K. Anderson, T. M. Biewer, B. E. Chapman, D. J. Den Hartog, C. B. Forest, S. C. Prager, D. L. Brower, and Y. Jiang, *Phys. Rev. Lett.* **85**, 2120 (2000).
- ³⁹P. M. Bellan, *Phys. Rev. Lett.* **57**, 2383 (1986).
- ⁴⁰R. D. Hazeltine and J. D. Meiss, *Plasma Confinement* (Addison-Wesley, Redwood City, CA, 1992).
- ⁴¹B. E. Chapman, J. W. Ahn, A. F. Almagri, J. K. Anderson, F. Bonomo, D. L. Brower, D. R. Burke, K. Caspary, D. J. Clayton, S. K. Combs, W. A. Cox, D. Craig, B. H. Deng, D. J. Den Hartog, W. X. Ding, F. Ebrahimi, D. A. Ennis, G. Fiksel, C. B. Forest, C. R. Foust, P. Franz, S. Gangadhara, J. A. Goetz, M. C. Kaufman, J. G. Kulpin, A. Kuritsyn, R. M. Magee, M. C. Miller, V. V. Mirnov, P. D. Nonn, R. O'Connell, S. P. Oliva, S. C. Prager, J. A. Reusch, J. S. Sarff, H. D. Stephens, M. D. Wyman, and T. Yates, *Nucl. Fusion* **49**, 104020 (2009).
- ⁴²D. D. Schnack, D. C. Barnes, Z. Mikic, D. S. Harned, and E. J. Caramana, *J. Comput. Phys.* **70**, 330 (1987).